A&A 472, 497–507 (2007)
DOI: 10.1051/0004-6361:20077324

Astronomy & Astrophysics

Gas and dust spectra of the D' type symbiotic star HD 330036

R. Angeloni[1,2], M. Contini[2,1], S. Ciroi[1], and P. Rafanelli[1]

[1] Dipartimento di Astronomia, Università di Padova, Vicolo dell'Osservatorio 2, 35122 Padova, Italy
e-mail: [rodolfo.angeloni;stefano.ciroi;piero.rafanelli]@unipd.it
[2] School of Physics and Astronomy, Tel Aviv University, Tel Aviv 69978, Israel
e-mail: contini@post.tau.ac.il

Received 18 February 2007 / Accepted 10 May 2007

ABSTRACT

Aims. We present a comprehensive and self-consistent modelling of the D' type symbiotic star (SS) HD 330036 from radio to UV.
Methods. Within a colliding-wind scenario, we analyse the continuum, line, and dust spectra by means of SUMA, a code that simulates the physical conditions of an emitting gaseous cloud under the coupled effect of ionisation from an external radiation source and shocks.
Results. We find that the UV lines are emitted from high-density gas between thestars downstream of the reverse shock, while the optical lines are emitted downstream of the shock propagating outwards from the system. As regards the continuum SED, three shells are identified in the IR, at 850 K, 320 K, and 200 K with radii $r = 2.8 \times 10^{13}$ cm, 4×10^{14} cm, and 10^{15} cm, respectively, after adopting a distance to Earth of $d = 2.3$ kpc. Interestingly, all these shells appear to be circumbinary. Analysis of the unexploited ISO-SWS spectrum reveals that both PAHs and crystalline silicates coexist in HD 330036, with PAHs associated to the internal shell at 850 K, and crystalline silicates stored in the cool shells at 320 K and 200 K. Strong evidence that crystalline silicates are shaped in a disk-like structure is derived on the basis of the relative band strengths. Finally, we suggest that shocks can be a reliable mechanism for activating the annealing and the consequent crystallisation processes.
Conclusions. We show that a consistent interpretation of gas and dust spectra emitted by SS can be obtained by models that account for the coupled effect of the photoionising flux and of shocks. The VLTI/MIDI proposal recently accepted by ESO aims to verify and better constrain some of our results by means of IR interferometric observations.

Key words. stars: binaries: symbiotic – stars: individual: HD 330036

1. Introduction

Symbiotic systems (SS) are interacting binaries composed of a hot star, generally a white dwarf (WD), a cool giant, and emitting nebulæ created by both the photoionising flux from the WD and by collision of the winds. On the basis of the near-infrared (NIR) colours, a classification into two types, S and D, was originally proposed by Webster & Allen (1975) according to whether the cool star (S type) or dust (D type) dominates the 1−4 μm spectral range. Some years later Allen (1982) introduced a third class, designated as D' type, characterised by very red colours in the far infrared (FIR) and by a cool star of spectral type F or G, in contrast to ordinary symbiotics where the cool giant is a M-type star (S type) or a Mira variable (D type). The D' types are quite rare objects, and nowadays only eight out of about 200 SS are known to belong to this class (Belczyński et al. 2000).

In the past years several studies allowed the distinctive features of D' types to be highlighted: for instance, both Smith et al. (2001) and Munari et al. (2001) showed that these stars display enhancements of the s-process elements that are synthesised via slow neutron captures during stellar evolution along the asymptotic giant branch (AGB). Moreover, when measuring the rotational velocity of the cool star, Pereira et al. (2005, hereafter P05) and Zamanov et al. (2006, hereafter Z06), point out that in the D' type SS the cool component rotates faster than the isolated giants, at a substantial fraction of the critical velocity (e.g. $v \sin i \sim 0.6\, v_{\rm crit}$ in the case of HD 330036). This high rotational velocity can result in high mass-loss rates, very likely enhanced in the equatorial regions, and will inevitably affect the dusty environment (Soker 2002) by leading to a disk-like circumbinary structure in which the high gas density enhances dust formation and growth. It would be the dust temperature stratification in such a disk, already noticed in some D' SS (e.g. V417 Cen, Van Winckel et al. 1994), that is the origin of the observed IR excess. Furthermore, under the hypothesis that the D' type orbits are synchronised, Z06 argue that the orbital periods would be relatively short (4−60 days) and the interbinary distance about 2−5 times the cool star radius.

One of the most intriguing aspects of the symbiotic phenomenon in these cases pertains to the dusty environment. These systems show a broad IR excess that has been attributed to emission from circumstellar dust, since the first IR surveys. While in D type objects the dust excesses have colour temperatures near 1000 K (Feast et al. 1983), in the D' SS their presence is revealed only beyond ∼3 μm, suggesting a lower temperature, which Allen (1984) claimed was not higher than 500 K.

Whatever symbiotic type (D or D') it may be, it was soon realized thanks to the development of IR astronomy, that it was difficult to explain the observed IR spectrum by a single temperature component, and theoretical models also, confirmed that several "dust" temperatures should be combined to reproduce the NIR-MIR data (e.g. Anandarao et al. 1988; Schild et al. 2001; Angeloni et al. 2007, in preparation).

As regards the emission line spectra, D'-type SS closely resemble planetary nebulæ (PN), leading to a long controversy about the exact evolutionary status of these stars. It is noteworthy that D' types were even classified by some authors

as young, compact PN with a binary core (Feibelman 1983, 1988; Lutz 1984, hereafter L84; Bhatt 1989; van Winckel et al. 1994; Corradi et al. 1999). However, Schmeja & Kimeswenger (2001) point out that the NIR colours provide a reliable tool for distinguishing symbiotic from genuine PN. Finally, based on the ongoing interaction between the cool giant and the nebula, Schmid & Nussbaumer (1993, hereafter SN93) favour a classification of D'-type systems as SS. Among D'-type SS, one of the most intriguing objects is HD 330036 (CN 1-1). Unfortunately, many physical parameters of this enigmatic system remain inconclusive.

The estimate of the hot-star temperature, for instance, ranges from 60 000 K (SN93), 10^5 K (L84), up to 2.5×10^5 K (Bhatt & Mallik 1986, hereafter BM86). The interpretation of polarisation measurements is also uncertain. In fact, Schulte-Labdeck & Magalhaes (1987) considered the polarisation observed (∼3%) in HD 330036 to have a purely interstellar origin; whereas Bhatt (1989) argued that, at least to some extent, the polarisation can be intrinsic to the system and due to scattering by dust grains in an asymmetric nebula, calling for a bipolar morphology.

More debatable is the distance to Earth, an important parameter in the context of this paper. L84 estimated a distance of ∼450 pc based upon the colour excess versus distance for stars within 20′ of HD 330036; but based on the cool star luminosity, there are several arguments that led P05 to assume a distance of 2.3 kpc, the difference between the estimates of L84 and P05 being in someway caused by different values of the reddening. Summarising, the probable limits for the distance to HD 330036 lie within ∼0.6 to 2.3 kpc, with upper values more likely.

On the other hand, the cool star is rather well-known even though its evolutionary status is still controversial: P05 obtained $L = 650\ L_\odot$, $T_{\rm eff} = 6200 \pm 150$ K, $\log g = 2.4 \pm 0.7$ where L is the luminosity, $T_{\rm eff}$ the effective temperature, g the gravity.

This implies $R_{\rm g} = 22\ R_\odot$, $M_{\rm g} = 4.46\ M_\odot$ (using $R_{\rm g}$ and $\log g$), and $P_{\rm rot} \leq 10.4 \pm 2.4$ d, where $R_{\rm g}$, $M_{\rm g}$, and $P_{\rm rot}$ stand for radius, mass, and rotational period, respectively.

These parameters would be theoretically sufficient for an estimate of the mass-loss rate (not found in the current literature), but the problem is to understand if the formulæ for dust-enshrouded red giants and supergiants and for oxygen-rich AGB stars remain valid when extended to a G-F giant. As a matter of fact, when we attempt to calculate $\dot{M}$ by using several proposed relations (Wachter et al. 2002; van Loon et al. 2005) and assuming the Pereira's stellar parameters, we find discordant results. Furthermore these values are too low ($\dot{M} < 10^{-9}\ M_\odot$/yr) to sustain any interaction of the binary stars that must be at the origin of the observed symbiotic activity (Kenyon 1988). Unfortunately, modelling of motions in the atmospheres of yellow giants and supergiants only manage to emphasise that the subject is still not well-understood, resulting in the lack of reliable empirical mass-loss rates or terminal wind velocities for normal G-F giants and supergiants (Achmad et al. 1997). For this reason we decided to attempt a completely alternative approach (Kemper et al. 2001) by deriving the mass loss rate by means of the crystalline dust feature recognisable in the infrared spectrum (see Sect. 5.3.4).

Allen (1984) realized the uniqueness of the dusty environment of HD 330036 among the known symbiotic stars in exhibiting infrared emission bands at 3.3 and 11.3 μm, suggesting a C-rich nature for this object. On the basis of IRAS observations BM86 noticed that there were two distinct components of infrared emitting dust in HD 330036: one at a temperature of ∼215 K and the other much hotter at ∼850 K. Interestingly, in order to obtain a likely dust-to-gas ratio, these authors postulated the existence of large dust grains ($a_{\rm gr} > 1$ μm).

In the present paper we aim to model HD 330036 in the light of the now widely accepted interpretation of SS as colliding-wind binary systems, by combining UV and optical observations (reported in L84 and SN93), together with the IR ISO-SWS (Short Wavelength Spectrograph) spectrum, analysed here for the first time. The observed line ratios allow us to constrain the physical conditions in the emitting nebulae, while the ISO data, combined with other IR photometry points from IRAS and 2MASS, reveal the properties of dust by constraining temperature, size, and chemical composition of the HD 330036 dusty environment.

We start by analysing the HD 330036 UV and the optical line spectra in Sect. 3. Subsequently, cross-checking the continuum and line ratio results, we select the models that best explain the gas and dust emission. We then derive the grain conditions and location by comparing the dust-reprocessed radiation flux with the IR data (Sect. 4). In Sect. 5 we review the main characteristics of dust features by carefully analysing the ISO-SWS spectrum. Discussion and concluding remarks follow in Sect. 6.

2. The models

2.1. The colliding-wind scenario

In the past years, theoretical models (Girard & Willson 1987; Kenny & Taylor 2005), as well as observations (Nussbaumer et al. 1995), have categorically shown that in SS both the hot and cool stars lose mass through stellar winds that collide within and outside the system, hence creating a complex network of wakes and shock fronts that result in a complicated structure of gas and dust nebulæ (Nussbaumer 2000).

In this paper, as previously done for other SS (e.g. Angeloni et al. 2007a), we refer to two main shocks: the one between the stars facing the WD, which is a head-on shock (hereafter the *reverse* shock), and the head-on-back shock, which propagates outwards the system (hereafter the *expanding* shock). Both the nebulae downstream of the shock fronts are ionised and heated by the radiation flux from the hot star and by shocks. The photoionising radiation flux reaches the shock front of the reverse shock, while it reaches the edge opposite to the shock front downstream of the expanding shock. This scenario is even more complicated in D' type systems by the giant fast rotation that leads to extended disk-like structures, both predicted (Z06) and, in some objects, even optically resolved (van Winckel et al. 1994).

The optical spectrum contains several forbidden lines whose ratios constrain the models. The characteristic electron densities indicate that the region where these lines arise is essentially different from the region that emits the UV lines. Thus we suggest that the optical spectrum results from the collision of the cool component wind with the ISM, in the external region of the disk or even outside, most probably throughout jets. This hypothesis will be tested by modelling the spectra. UV lines corresponding to high densities ($>10^6$ cm^{-3}) are generally emitted from the nebula downstream of the reverse shock between the stars (e.g. Contini & Formiggini 2003; Angeloni et al. 2007a).

2.2. The SUMA code

The results presented here are performed using SUMA (Viegas & Contini 1994; Contini 1997), a code that simulates the physical conditions of an emitting gaseous cloud under the coupled

Table 1. The UV and optical emission lines.

Line	Obs[1]	m1	Obs[2]	m2	m3	Line	Obs[1]	m4	m5	m6
NV 1239	1.46 ± 0.32	1.68	–	0.04	0.09	[OII] 3727+	10 ± 5	8.	4.	6.3
NIV 1468	6.02 ± 0.81	7.66	4.3	5.8	7.3	[NeIII] 3869+	200 ± 50	197.	140.	155.
CIV 1548	48.9 ± 4.57	44.8	46.	40.0	44.7	[CIII] 4068	<5 ± 4	0.07	0.07	3[5]
HeII 1640	1.65 ± 0.25	2.28	1.1:	0.9	0.3	HI 4340	40 ± 11	46.	45.	45.
OIII] 1662	5.61 ± 0.76	4.8	5.3	4.4	4.25	[OIII] 4363	70 ± 18	50.	71.	84.
NIII] 1750	6.12 ± 0.71	5.0	5.7	4.8	5.03	HeI 4471	<5 ± 4	4.4	5.7	6.
CIII] 1911	19.11 ± 1.51	19.6	21.	19.2	19.2	HeII 4686	5 ± 4	18.	9.	6.3
Hβ4861	–	2	–	2	1.5	Hβ4861	100	100	100	100
Hβ4861[3]	–	1.75	–	2.5	2	Hβ4861[4]	–	6.57	0.15	0.098
–	–	–	–	–	–	[OIII] 5007+	1145	1150	970.	1074.
V_s(km s^{-1})	–	300	–	150.	150.	–	–	30.	50.	50.
n_0 (10^6 cm^{-3})	–	2	–	40.	40.	–	–	0.15	0.15	0.15
B_0 (10^{-3} gauss)	–	1	–	1	1	–	–	1	1	1
T_*(10^5 K)	–	1.04	–	0.6	0.6	–	–	1.04	0.6	0.6
U	–	10	–	4.5	4.	–	–	0.007	0.013	0.08
d/g (10^{-4})	–	12	–	4	0.2	–	–	20	4	0.04
a_{gr}(μm)	–	0.2	–	0.2	2.	–	–	0.2	0.2	2.
C/H (10^{-4})	–	5.3	–	5.3	5.3	–	–	3.3	3.3	3.3
N/H (10^{-4})	–	5.1	–	5.1	5.1	–	–	0.91	0.91	0.91
O/H (10^{-4})	–	7.6	–	7.6	7.6	–	–	6.6	6.6	6.6

[1] Fluxes in 10^{-12} erg cm^{-2} s^{-1} (Lutz 1984); [2] fluxes in 10^{-12} erg cm^{-2} s^{-1} (Schmid & Nussbaumer 1993); [3] absolute fluxes in 10^5 erg cm^{-2} s^{-1}; [4] absolute fluxes in erg cm^{-2} s^{-1}; [5] blended with [SII].

effect of ionisation from an external radiation source and shocks and in which both line and continuum emission from gas are calculated consistently with dust reprocessed radiation. Grain heating and sputtering processes are also included. The derived models have been successfully applied to several SS, e.g. AG Peg (Contini 1997, 2003), HM Sge (Formiggini et al. 1995), RR Tel (Contini & Formiggini 1999), He2-104 (Contini & Formiggini 2001), R Aqr (Contini & Formiggini 2003), H1-36 (Angeloni et al. 2007b), as well as to nova stars (V1974, Contini et al. 1997 – T Pyx; Contini & Prialnik 1997), and supernova remnants (e.g. Kepler's SNR, Contini 2004).

The calculations start with gas and dust entering the shock front in a steady state regime where the gas is adiabatically compressed and thermalised throughout the shock front. In the downstream region the compression is derived by solving the Rankine-Hugoniot equations (Cox 1972), in which the downstream region is automatically divided into plane parallel slabs in order to calculate the physical conditions as smoothly as possible throughout the nebula. Radiation transfer and optical depths of both continuum and lines are calculated for a steady state; in particular, radiation transfer of the diffused radiation is taken into account following Williams (1967). The fractional abundance of the ions in different ionisation stages is calculated in each slab by solving the ionisation equilibrium equations for the elements H, He, C, N, O, Ne, Mg, Si, S, Cl, Ar, and Fe. The electron temperature in each slab is obtained from the energy equation when collisional processes prevail and by thermal balancing when radiation processes dominate. Compression downstream strongly affects the gas cooling rate by free-free, free-bound, and line emission; consequently, the emitting gas will have different physical conditions, depending on the shock velocity and on the pre-shock density.

Dust is included in the calculations, too. Dust and gas are coupled throughout the shock-front and downstream by the magnetic field. In each slab, the sputtering of the grains is calculated, leading to grain sizes that depend on the shock velocity and on the gas density. The temperature of the grains, which depends on the grain radius, is then calculated by radiation heating from the external (primary) source and by diffuse (secondary) radiation, as well as by gas collisional heating. The dust-reprocessed radiation flux is calculated by the Plank-averaged absorption coefficient of dust in each slab and integrated throughout the nebula downstream.

The input parameters that characterise the shock are the shock velocity, V_s, the preshock density of the gas, n_0, and the preshock magnetic field, B_0. The radiation flux is determined by the temperature of the star, interpreted as a colour temperature, T_*, and by the ionisation parameter, U. The dust-to-gas ratio, d/g, is also accounted for, as well as the relative abundances of the elements to H.

A detailed description of the updated code is to be presented in Contini & Viegas (2007 in preparation).

3. The line spectra

Low-resolution (~7 Å) IUE spectra were taken in 1979 September, 1980 June, and 1981 April (L84), while optical spectra were obtained on the 4 m and 1 m telescopes at Cerro Tololo Inter-American Observatory (CTIO) during 1977, 1978, and 1979 (L84). The IUE observational data by SN93 were taken in 1984 July 26. The observed UV and optical lines are shown in Table 1.

3.1. The UV lines

The data come from L84 and from SN93. Notice that the two spectra in the UV (left side of Table 1) observed at different times show compatible line ratios, considering that the Lutz (L84) spectrum is reddening-corrected while Schmid & Nussbaumer (SN93) give the observed fluxes. However, the NV 1239 line that was observed by Lutz is absent in the SN93 spectrum. This is a crucial line, which can be explained not only by a higher T_*, but also by a relatively high shock velocity. Indeed, the shock velocity is responsible for the heating of the gas downstream in the immediate post shock region where $T \propto V_s^2$.

We calculated the spectra by different models, m1, m2, and m3 (Table 1, bottom). Model m1 leads to the best fit of the calculated line ratios to those observed by Lutz and is characterised by a high V_s (300 km s^{-1}) and a high T_* (100 000 K). Model m2 explains the line ratios observed by Schmid & Nussbaumer, who derived a temperature of the hot star T_* = 60 000 K. Such a relatively low temperature is valid for explaining the UV spectra that do not show lines from relatively high ionisation levels (e.g. NV). Model m3 is characterised by a large a_{gr}, which is consistent with crystalline grain formation (see Sects. 4 and 5). The relatively high magnetic field adopted ($B_0 = 10^{-3}$ Gauss) is characteristic of SS (e.g. Crocker et al. 2001). Notice that changing one input parameter implies the readjustment of all the other ones.

The models that explain the UV line ratios correspond to different temperatures of the hot star and different grain radii. Both T_* = 100 000 K and V_s = 300 km s^{-1}, which are used in model m1 to explain the UV spectrum observed by Lutz, particularly the NV 1240 line flux, are less suitable because such high velocities are not seen in the FWHM profiles. Moreover, T_* = 100 000 K leads to HeII4686/Hβ, so higher by a factor of ∼3 than observed in the optical domain. By adopting T_* = 60 000 K, both the UV line spectra (SN93) and the optical ones (L84 – see Sect. 3.2) are satisfactorily explained. Higher preshock densities are adopted by models m2 and m3 to compensate for the lower compression downstream that results from a lower V_s (=150 km s^{-1}). Notice that the shock velocity is higher in the reverse shock (V_s = 150 km s^{-1}) than in expanding shock (V_s = 50 km s^{-1}). The velocity of the reverse shock is rather high (V_s = 150−300 km s^{-1}) compared with the ones obtained from the radial velocity measurements by L84 (Table 5 therein), which are ∼12−16 km s^{-1}. The densities in the reverse shock are too high to contribute to the optical forbidden lines (e.g. [OII]).

The model input parameters are shown at the bottom of Table 1. The relative abundances C/H, N/H, and O/H appear in the last rows. The other elements (H, He, Ne, Mg, Si, S, Ar, Fe) are adopted with solar abundance (Allen 1973) because no lines are available for these elements. Indeed, P05 indicate a near solar Fe/H. The relative abundances adopted for models m1, m2, and m3, consistently calculated, are C/O = 0.70, N/O = 0.67, and C/N = 1.04 in the reverse shock, while L84 found C/O = 0.79 and N/O = 1.00 and SN93 C/O = 0.73, N/O = 0.67, and C/N = 1.1. The relative abundances of C, N, and O adopted to reproduce the UV spectra are in good agreement with those obtained by SN93 for symbiotic stars. Moreover, the models lead to CIII]1909/SiIII]1892 < 1, which indicates that HD 330036 is less adapted to the PN class.

3.2. The optical lines

The optical spectra observed by Lutz (Table 1, right) contain several forbidden lines that refer to relatively low critical densities for deexcitation, particularly the [OII] lines. The radial velocities observed by Lutz are rather low and applicable to those found in the winds close to the giants, typical of 20−30 km s^{-1}. The densities tend to decrease with distance from the giant centre; therefore, the outward shocks most likely accompany the wind close to the system.

Lutz found that the emission line region is characterised by electron densities $n_e \sim 10^6$ cm^{-3} and temperatures of $T_e \sim 1.5 \times 10^4$ K. Actually, the weakness of the [OII] lines compared to the [OIII] lines and the strong [OIII] 4363 line are indicative of relatively high T_e and n_e. The presence of strong optical forbidden lines constrains the density to $\leq 10^6$ cm^{-3}. Recall that the densities downstream are higher than the pre-shock ones by about a factor of 10 due to compression. The agreement of the calculated optical line ratios with the data, adopting solar abundances, indicates that the shock is sweeping up the IS matter. Moreover the models lead to grain temperatures <100 K.

The results of model calculations reproduce the data within the errors (20−30%), except for the observed HeII 4686 line in model m4, which is overpredicted by a factor of ≥3; therefore, this model is less reliable. In Fig. 1 the profiles of the electron temperature and density downstream of the reverse shock (left) and of the expanding shock (right) are given, as well as the distribution of the fractional abundance of the most significant ions (bottom panels). The photoionising source (hot star) is on the left for all diagrams; therefore, the distance scale is logarithmic and symmetrical with respect to the centre of the nebula with the highest resolution towards the edges of the nebula, in the diagrams on the right of Fig. 1, which refer to the case in which the photoionising flux and the shock act on opposite edges. In the top diagrams, models m1 (left) and model m4 (right) appear. Notice that in the nebula downstream of the reverse shock represented by model m1, sputtering is very strong and the grains are destroyed after a short distance from the shock front. In the middle diagrams, the physical conditions for models m2 (left) and m5 (right) are described, while the lower diagrams refer to models m3 (left) and m6 (right). The comparison between the middle and bottom diagrams shows that relatively large grains (a_{gr} = 2 μm) affect the distribution of the physical conditions downstream, particularly the distribution of the ions.

The d/g ratios are selected by cross-checking the modelling of the continuum. A high d/g enhances the cooling rate downstream, changes the distribution of the physical conditions, and consequently the emitted line intensities.

4. The continuum SED

In Fig. 2 we present the modelling of the continuum SED. The data in the IR come from the ISO archive (see Sect. 5 for more details), the IRAS Catalogue of Point Sources, and the 2MASS database, while the data in the UV are extracted from the IUE archive and refer to the 1984 spectrum already analysed by SN93. The radio points are from Milne & Aller (1982) and the optical ones (B and V Johnson magnitude) from Kharchenko (2001).

The SED of the continuum results from the contributions of the fluxes from the cool and hot stars, as well as the fluxes from the dust shells, the bremsstrahlung from the ionised nebulae downstream of the shock fronts (which emit the UV and optical line spectra), and the reprocessed radiation from dust. As a first guess, the flux from the stars and the dust shells is approximated by black body radiation. We find that a black body of 6000 K fits the NIR data corresponding to the cool star, in agreement with P05, while the temperature of the hot star is calculated phenomenologically by modelling the line spectra (Sect. 3).

4.1. The shells

The dust grains form in the atmosphere of the giant star where the temperature has dropped below ∼2000 K and the densities are $\sim 10^9 - 10^{10}$ cm^{-3}. Their temperature results from the coupled effect of the photoionisation flux from the WD and collisional heating by the gas. The flux emitted from the region closer to the shock front downstream, which corresponds to the maximum temperature of dust, is calculated by the Plank-averaged absorption coefficient of dust. The cooling rate is very strong

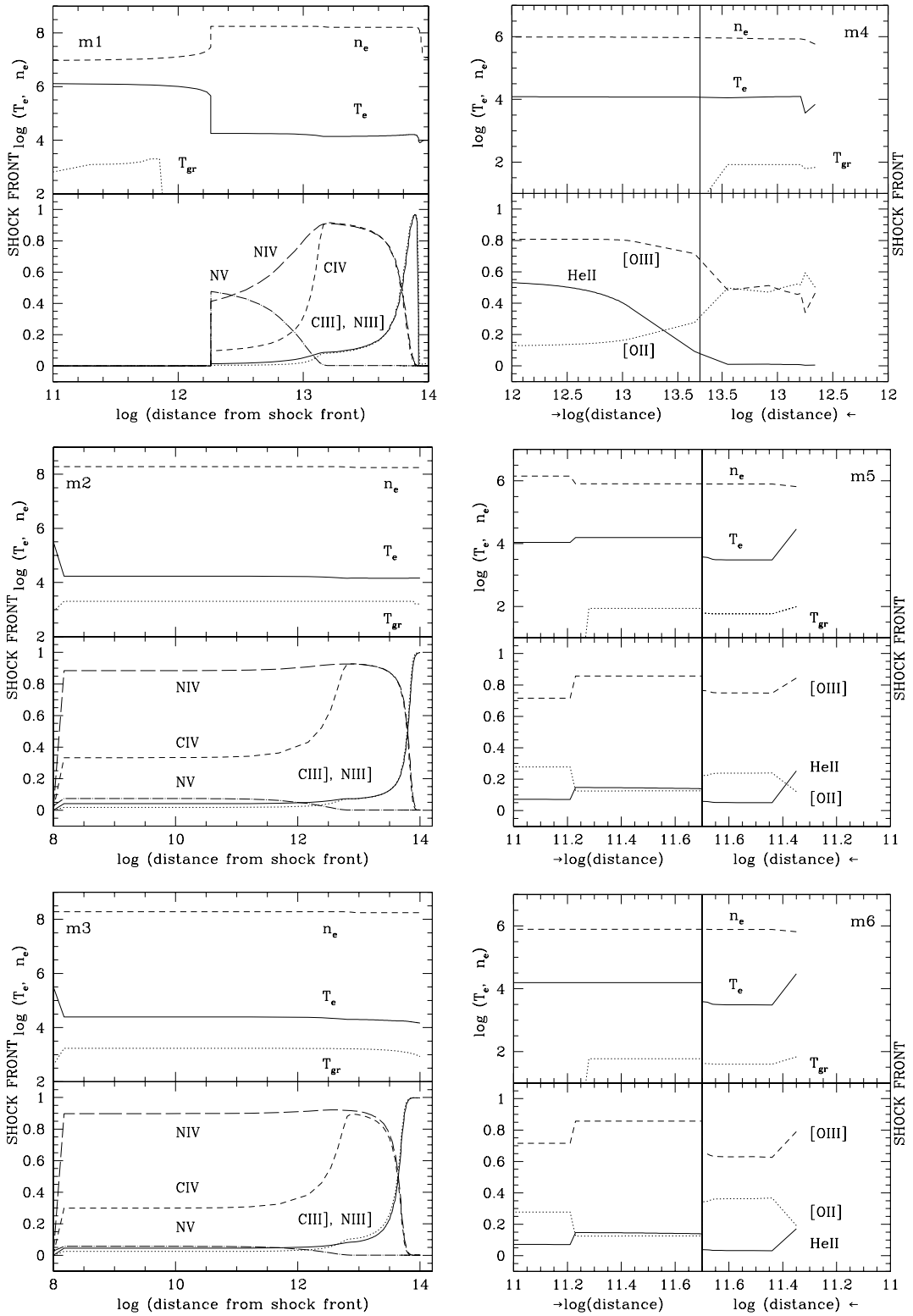

Fig. 1. *Top left diagram*. *Top panel*: the profile of the electron temperature (solid line), of the grain temperature (dotted line), and of the electron density (dashed line) downstream of the reverse shock for model m1. *Bottom panel*: the distribution of the fractional abundance downstream. *Top right diagram*: the same downstream of the expanding shock for model m4. *Middle left diagram*: the same for model m2. *Middle right diagram*: the same for model m5. *Bottom left diagram*: the same for model m3. *Bottom right diagram*: the same for model m6.

downstream at such densities; therefore, the flux from the shell corresponds mainly to the maximum temperature of the grains and can be modelled by a black body. The temperature of the dust shells is derived by modelling the ISO and IRAS data, which agree in the overlapping frequency range. This suggests that variability, at least in the IR domain, has not been so large as to substantially modify the dust continuum emission. Figure 2 diagrams show that the data can be explained by the combination of at least three black body (bb) fluxes, corresponding to temperatures of 850 K, 320 K, and 200 K.

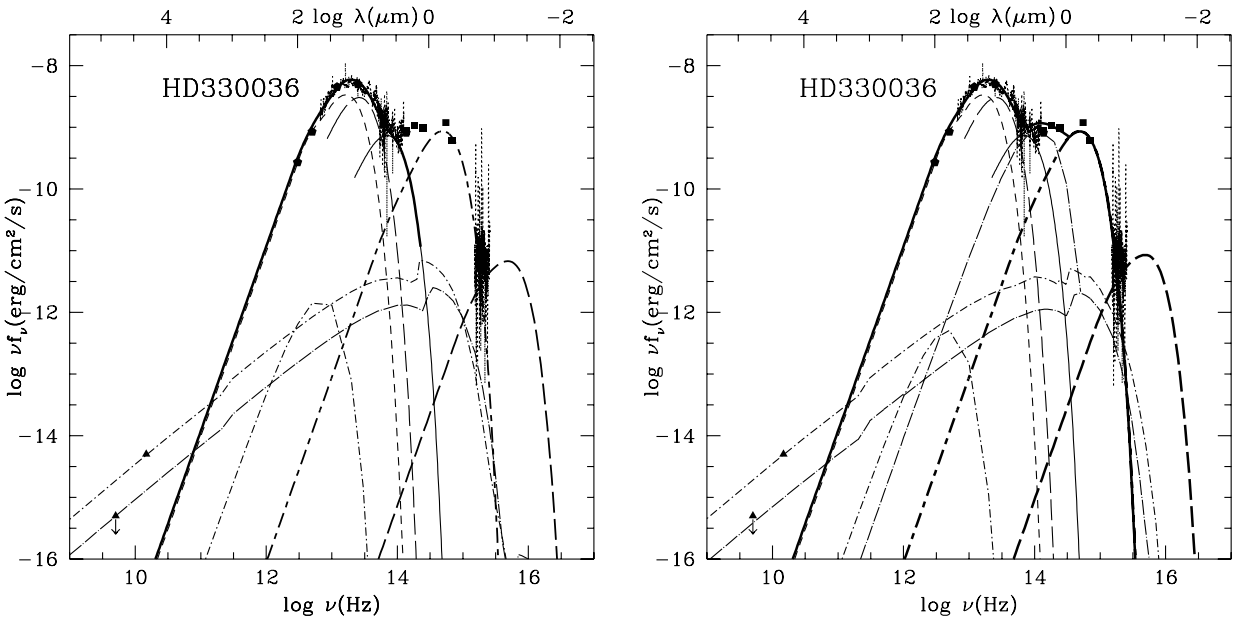

Fig. 2. The SED of the continuum. Data (black squares) from the IUE archive (UV range), from the ISO archive, IRAS catalogue of Point Sources and 2MASS database (IR range), from Kharchenko (2001) (*B* and *V* Johnson magnitude), and from Milne & Aller 1982 (black triangles – radio range). The bb at 60 000 K (thick long-dashed); the bb at 6000 K (thick long-short dashed); the bb at 850 K (thin solid); the bb at 320 K (thin long-dashed); the bb at 200 K (thin short-dashed). *Left diagram*: the bremsstrahlung calculated by model m2 (long-dash dot); the bremsstrahlung and relative dust emission by model m5 (short-dash dot); the summed SEDs of the dust shells (thick solid). *Right diagram*: the bremsstrahlung and relative dust emission calculated by model m3 (long-dash dot); the bremsstrahlung and relative dust emission by model m6 (short-dash dot); the summed SEDs of the dust shells, reemission by dust from the reverse shock, and the cool star bb (thick solid).

By comparing the models with the data, we obtain the η factors: they depend on the radius of the dust shell, r, and on the distance of the system to Earth d ($\eta = r^2/d^2$), being the fluxes calculated at the nebula and the data measured on Earth. Adopting d = 2.3 kpc, we find $r = 2.8 \times 10^{13}$ cm, 4×10^{14} cm, and 10^{15} cm for the shells at 850 K, 320 K, and 200 K, respectively. Interestingly, this implies that all the dust shells are circumbinary, with the coolest ones extending well beyond the two stars if we assume an upper limit for binary separation of $\sim 8 \times 10^{12}$ cm (5 R_g), as suggested by Z06. According to the D' type nature of this star, the dust shell at ~1000 K generally observed in D type SS does not appear in HD 330036.

4.2. The shocked nebulæ

The radiation emitted from the shocked nebulae accounts for both bremsstrahlung and dust-reprocessed radiation, which are calculated consistently in the downstream region. The fluxes are integrated from the shock front throughout regions of gas and dust in different physical conditions. The reradiation IR bump from dust is in fact wide because it accounts for the stratification of the temperature downstream. The bremsstrahlung covers a wide wavelength range, from radio to UV.

In the previous sections we have presented some alternative models, which were selected from the best fit of the line spectra. Since the models m1 and m4, calculated adopting a hot star temperature of $T_* \sim 10^5$ K, fail in reproducing the HeII 4686/Hβ ratio, we consider only the remaining ones (Table 1) in the following. The continua calculated by these models are compared with the observations in the diagrams of Fig. 2. In the left one the models m2 and m5 appear, representing the nebulae downstream of the reverse and of the expanding shock respectively, and calculated with a hot star temperature of T_* = 60 000 K and an initial grain radius a_{gr} = 0.2 μm; while the right one, show models m3 and m6, calculated with T_* = 60 000 K and a_{gr} = 2 μm. Models with μm-size grains are justified by the presence of silicate crystalline features (e.g. Vandenbussche et al. 2004) at the top of the IR continuum, as we will discuss in details in Sect. 5.3. In Fig. 2 diagrams we have also added the UV data in order to constrain the bremsstrahlung fluxes in the UV range, while the modelling of the IR data is constrained by the d/g ratios. The calculated line ratios and the continuum were then cross-checked until both the line spectra and the SEDs were fitted satisfactorily.

The SED of the bremsstrahlung is constrained by the radio data, and the dust reradiation peak by the IR data in the 1−3 μm range. Generally in D-type SS the cool star is of Mira type with temperatures of 2000−3000 K, so their fluxes cover the data in the NIR range. However, HD 330036 shows a cool star temperature of 6000 K, therefore adopting the bb approximation, the emission-peak results shifted toward higher frequencies and the 1−3 μm continuum data are most probably explained by hot dust.

The right diagram of Fig. 2 shows that the contribution of the reprocessed radiation of dust from the shocked nebula downstream of the reverse shock (m3) is significant in this range, while the grains downstream of the reverse shock calculated with a_{gr} = 0.2 μm (m2) reach temperatures of ~1900 K and easily evaporate; therefore, model m2 is not significant in the modelling of the hot dust. The contribution of the dust downstream of the expanding shock, which reaches temperatures of ~100 K, cannot be seen in the SED because it is hidden by the dust shell radiation flux.

The d/g ratio for models m2 and m5 is 4×10^{-4}, of the order of d/g in the ISM; for models m3 and m6 the d/g ratio is even lower, being reduced by factors >10. Recall that dust emissivity at a temperature T_d is calculated by $4\pi\ a_{gr}^2\ B(\lambda,T_d)\ d/g\ n_{gas}$

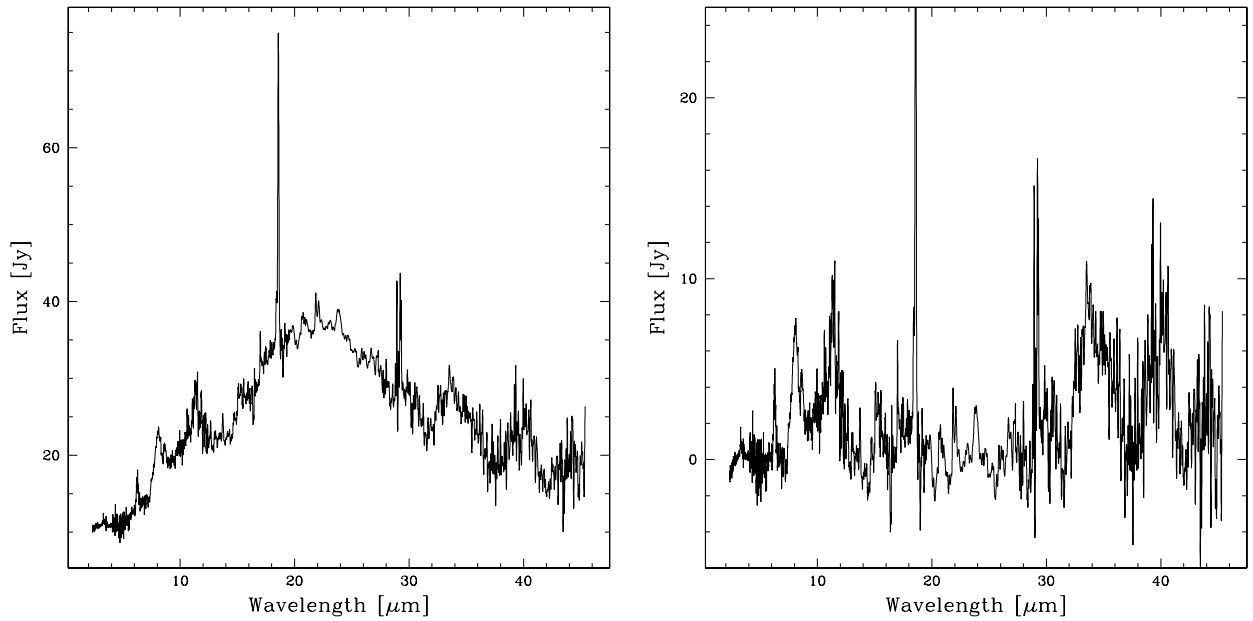

Fig. 3. *Left*: ISO-SWS spectrum of HD 330036. The strongest spectral features at ∼18 μm and ∼28 μm are instrumental artifacts (see Sect. 5.1). *Right*: continuum-subtracted ISO-SWS spectrum of HD 330036. Notice the bands usually attributed to polycyclic aromatic hydrocarbons (at 3.3, 6.2, 8 and 11.3 μm). At longer wavelengths we found evidence of emission from crystalline silicates (clearly visible in the strong complexes at ∼33 μm and ∼40 μm).

(Viegas & Contini 1994), where $B(\lambda,T_{\rm d})$ is the Plank function. A lower d/g, which is constrained by the data, compensate for a higher $a_{\rm gr}$. Therefore, in the two diagrams of Fig. 2, which account for models calculated by different $a_{\rm gr}$, the intensities of the reradiation peak of dust relative to bremsstrahlung are similar.

We can now calculate the radius of the nebulae by the η factors. Adopting d = 2.3 kpc and models m2 and m5, the reverse shock and the expanding shock have $r = 1.9 \times 10^{13}$ cm and $r = 4.9 \times 10^{15}$ cm respectively, while adopting models m3 and m6 the reverse and expanding shocks have radius $r = 1.8 \times 10^{13}$ cm and $r = 8.7 \times 10^{16}$ cm, respectively. It is worth noticing that the reverse shock radius is an upper limit because we have adopted the maximum value for the distance (d = 2.3 Kpc), and the η is constrained by the datum at 5 GHz, which in turn is an upper limit. Figure 1 (bottom left) shows that the temperature of dust calculated with model m3 is ≤1500 K at a distance $>10^{12}$ cm from the shock front, in agreement with a shell radius of $\sim 10^{13}$ cm calculated from the η factor by fitting the SED in Fig. 2 (right diagram).

Finally, the datum at 14.7 GHz in the radio range constrains the bremsstrahlung, whereas the other one at 5 GHz is just an upper limit (Milne & Aller 1982). Incidentally, the physical conditions downstream of models m1, m2, and m3, representing the reverse shock, lead to an optical thickness $\tau > 1$ at $\nu < 10^{12}$ Hz (Osterbrock 1988), indicating that self absorption of free-free radiation reduces the flux. On the other hand, the conditions downstream of models m4, m5, and m6, which represent the expanding shock, lead to $\tau < 1$ at 14.7 GHz but to $\tau \geq 1$ at 5 GHz.

Summarising, we have found that the physical parameters that best explain the shocked nebulae are $T_* = 60\,000$ K, $V_{\rm s} = 150$ km s^{-1}, $n_0 = 4 \times 10^7$ cm^{-3}, $a_{\rm gr} = 0.2$ μm for the reverse shock, while for the expanding shock we found $V_{\rm s} = 50$ km s^{-1}, $n_0 = 1.5 \times 10^5$ cm^{-3} and grains of both sizes, $a_{\rm gr} = 0.2$ μm and 2 μm.

5. The solid state features in the ISO spectrum

5.1. Observations and data reduction

HD 330036 was observed by ISO on 1996 September 18. In this paper we focus on the spectrum taken with the Short Wavelength Spectrograph (hereafter SWS – de Graauw et al. 1996), used in full-grating scan mode (AOT 01) and covering the wavelength range between 2.38 and 45.2 μm (Fig. 3, left). The spectrum comes from the "Uniform database of SWS 2.4–45.4 micron spectra" within the Highly Processed Data Products (HPDP) section of the ISO Archive. This database presents a complete set of all valid SWS full-scan 2.4–45.4 μm spectra processed (from the last stage of the pipeline software) and renormalised in as uniform a manner as possible. In particular, the processing produces a single spectrum for each observation from the 288 individual spectral segments, which are the most processed form available from the ISO archive (see Sloan et al. 2003, for details about the algorithm used to generate the database). However, some instrumental artifacts are still present (e.g. the strong "glitches" at ∼18 μm and ∼28 μm, whose profiles show a characteristic vertical flux increase followed by an exponential decrease, revealing their fake origin). Obviously, these features are not considered in deriving physical conclusions, and we point them out whenever the real origin of such structures remains ambiguous.

We analysed the data with the IRAF package software. In particular, we defined a continuum for the ISO-SWS spectrum by means of a spline-fit function: although this continuum does not necessarily have a physical meaning, it merely aims to enhance the sharp structures visible on top of the spectrum and to offer an easier identification of the solid state features. The continuum-subtracted spectrum of HD 330036 appears in Fig. 3, to the right. In spite of the low quality many dust bands are recognised, particularly at long wavelengths.

The spectrum appears substantially different with respect to the other SS ISO spectra analysed by Angeloni et al. (2007a),

where the mid-infrared range is dominated by the strong emission of amorphous silicate dust. Conversely, in HD 330036 it can be clearly split into two regions: the short wavelength one (up to ∼15 μm) dominated by PAH prominent emission bands and the long one showing a blending of narrow and characteristic emission profiles, often concentrated in specific wavelength regions (named *complexes*), whose carriers are believed to be crystalline silicates. Only after the ISO mission were these dust species noticed to be present outside our own solar system, for the first time allowing a mineralogical analysis of the dust composition in a wide range of astrophysical environments. In the following, we study the specific solid state features visible in the ISO-SWS spectrum.

5.2. PAHs

A wide variety of astronomical sources show some strong emission bands at 3.3, 6.2, 7.7, 8.6, and 11.3 μm: the so-called unidentified infrared (UIR) emission features (Puget & Leger 1989; Allamandola et al. 1989). Though some features remain still unidentified, the UIR spectrum as a whole is linked to PAHs, or to small grains containing PAHs, whose variety and complexity suggest a mixture of ionised and neutral PAH molecules. HD 330036 exhibits all these UIR bands (Fig. 4). In this section we analyse their profiles and peak positions, in order to investigate the PAH local conditions and formation history.

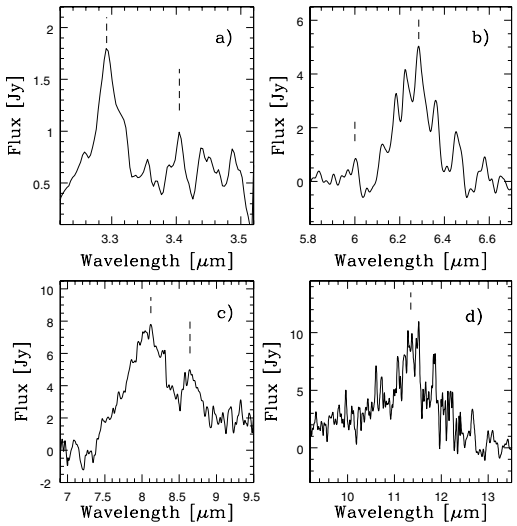

Fig. 4. The UIR bands in the spectrum of HD 330036: **a)** the 3.3 μm feature, **b)** the 6.2 μm feature, **c)** the 7.7 and 8.6 μm features, **d)** the 11.3 μm feature. The dashed lines indicate the band peak position.

5.2.1. The 3.3 μm feature

HD 330036 shows a prominent feature at ∼3.29 μm (Fig. 4a) usually attributed to the C-H stretching mode ($v = 1 \rightarrow 0$) of highly excited PAHs. The profile is clearly asymmetric, with the blue wing steeper than the red one. The peak position and the FWHM (3.292 and 0.037 μm, respectively) look similar to other 3.3 μm profiles seen in e.g. the Orion bar, even though these characteristics do not seem to be so common in astronomical sources (van Diedenhoven et al. 2004). A second weaker feature appears centred at ∼3.40 μm and is identified with the excitation of higher vibrational levels (Barker et al. 1987). There is unconvincing evidence of the other, weaker emission features at 3.44 and 3.49 μm.

According to laboratory studies concerning the role of the physical environment on the IR spectroscopy of PAHs (Joblin et al. 1994, 1995) and on the basis of the band profile, we suggest that the carriers of the 3.3 μm feature in HD 330036 are likely to be large PAH molecules, at rather high temperatures (∼800−900 K). Although far from conclusive, it is worth noticing the similarity between the observed "symbiotic" profile and the laboratory one of the ovalene molecule, as reported by Joblin et al. (1994, 1995).

5.2.2. The 6.2 μm feature

Even if this region of the spectrum is moderately noisy, we easily recognise the feature at ∼6.2 μm (preceded by a weak feature at about 6.0 μm), which is the PAH C-C stretching band (Fig. 4b). The precise peak position and the width of this emission feature are strongly influenced by several parameters, e.g. molecular size, molecular symmetry, charge status, dehydrogenation, etc. (Hudgins & Allamandola 1999; Bakes et al. 2001; Hony et al. 2001).

The overall shape of the profile, peaking at ∼6.25 μm and rather symmetric, suggests a link with objects such as some post-AGB and emission-line stars. According to e.g. Peeters et al. (2002), this symmetry could indicate that the PAH family emitting the band at ∼6.2 μm has not yet been exposed to a harsh radiation field and its composition still reflects the conditions during the formation at high temperatures.

This last remark, along with the temperature suggested by the 3.3 μm band, is consistent with our scenario proposing that PAHs within HD 330036 lie in the inner region ($T \sim 850$ K, $r \sim 2.8 \times 10^{13}$ cm) as found by modelling the SED (Sect. 4).

5.2.3. The 7.7 and 8.6 μm features

The "7.7 μm" feature in HD 330036 appears clearly redshifted with respect to standard positions observed in other astronomical sources (Peeters et al. 2002). Its profile seems to show several substructures (Fig. 4c); furthermore, the peak position is at ∼8.08 μm, and there is no apparent trace of the two main components seen in the "standard" profiles at ∼7.6 and ∼7.8 μm. The band resembles the one seen in the H-deficient Wolf-Rayet star (WR 48a), so that the whole feature could be a sort of blend of a "classical" 7.7 μm PAH feature and of a UIR band whose carriers seem likely to be amorphous carbon dust or large "pure" carbon molecules (Chiar et al. 2002). The band usually ascribed to C-H in plane bending vibrations of probably ionised PAHs at ∼8.64 μm is also present.

5.2.4. The 11.3 μm feature

The strongest PAH band in HD 330036 is the one at 11.3 μm, already noticed by Roche et al. (1983). This range of the spectrum (Fig. 4d) can show both the bands belonging to PAHs and to silicates. Moreover, unfortunately the S/N level of the detector is severely inadequate, so any firm conclusion based on the analysis of the profile is precluded. Nevertheless, some peaks and a plateau do not exclude the presence of some typical, intrinsic substructures.

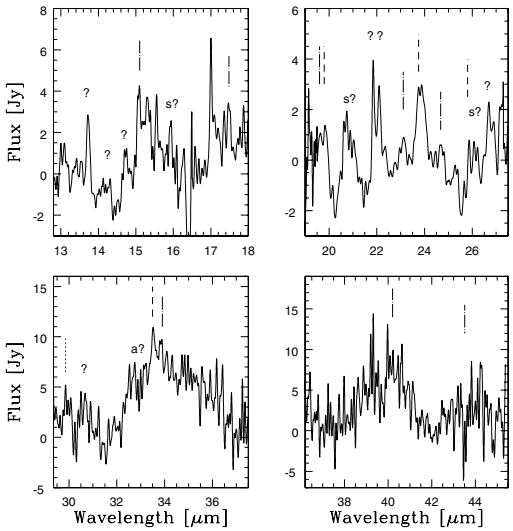

Fig. 5. Zoom of the spectrum of some interesting crystalline complexes. Short dashed line: fosterite; dot-dashed line: enstatite; dotted line: diopside; s: silica; a: anorthite; ?: bands whose attribution to a specific carrier is still doubtful.

5.3. Crystalline silicates

As stated above, the ISO-SWS spectrum beyond ∼15 μm shows the bands usually attributed to crystalline silicates. Despite the S/N level not being adequate throughout the whole spectral range (e.g. the instrumental band 3E at 27.5−29 μm is known for its mediocre performance), several features are clearly visible on top of the continuum, constraining the chemical compositions and spatial distribution of this symbiotic dust.

5.3.1. The observed crystalline bands

A zoom on some interesting crystalline complexes is shown in Fig. 5. Most of the bands can be confidently identified with crystalline olivine (i.e. fosterite – Mg_2SiO_4) around 19.7, 23.7, and 33.6 μm and with pyroxenes (i.e. enstatite – $MgSiO_3$) around 23.1, 24.6, 40.5, and 43 μm, whereas the features at ∼15.9, 20.7, and 26.1 μm seem to agree with silica (SiO_2).

Several bands still lack an identification (we label them with question marks in Fig. 5), thus suggesting the presence of more features, even though weaker and noisier. As already stressed in Sect. 5.1, some bands are rather controversial because they could originate from instrumental artifacts (e.g. the 13.8 and 14.2 μm features, with a contribution from enstatite that cannot be excluded). Furthermore, even when the actual origin of the features has been verified, it is not always easy to attribute them to some specific physical carriers (see, Molster et al. 2002b, Table 1): e.g., those at ∼20, 26, and 32 μm could fit the emission bands of diopside ($CaMgSi_2O_6$), as well as those of anorthite (i.e. at ∼26). However their relative strengths suggest that they would only represent minor components. Spectra with a higher S/N ratio and beyond the wavelength coverage of ISO-SWS are clearly needed to better constrain this composition insight.

5.3.2. A disk-like geometry for the silicate dust shell

After the end of the ISO mission, several studies pointed out that the high abundance of crystalline silicate seems to be related to the geometry of dust shells. In particular, the objects displaying strong crystalline bands (e.g. the olivine 33.6 μm band stronger than 20% over the continuum) are known to have highly flattened dust geometrical distributions (Molster et al. 1999a, 2002). The analysis of the crystalline silicate profiles in HD 330036 revealed that not only is the olivine 33.6 μm band stronger than 30% over the continuum, but its profile (with a secondary peak at 34.1 μm), along with the relative strength of the 23.0 and 23.7 μm features, also firmly suggests a disk-like geometry of the silicate envelope.

The existence of such a disk is also sustained by dynamical considerations of the orbital parameters of HD 330036 as a binary system. In fact, as noticed by Yamamura et al. (2000) for close-binary systems like ours, the massive interaction between the giant and the secondary star strongly affect the local environment, leading to the formation of a massive circumbinary disk in a rather short time. Finally, recall that a disk structure has already been proposed for another D' SS (V417 Cen) whose ring nebula has been optically resolved (Van Winckel et al. 1994).

5.3.3. Constraints on dust temperature

All crystalline silicates in evolved stars tend to show low temperatures (<300 K; Molster et al. 2002b). We thus suggest that the crystalline dust temperature in HD 330036 lies close to 100−200 K. Otherwise, in stark contrast to the case of higher temperatures (Molster et al. 2002), the strength ratio of the fosterite band at 33.6 and 23.7 μm would have been <1. This constraint on the temperature, along with the disk geometry deduced above, indicates that the crystalline silicates reside in the outer large circumbinary envelopes of dust that were found by modelling the IR SED in Sect. 4.

5.3.4. Constraints on the mass-loss rate of the cool star

As reported in the introduction, an estimate of the mass loss rate of the cool component of HD 330036 is not trivial. As the relations involving stellar atmosphere modelling are still not reliable (Achmad et al. 1997), we try a different method by exploiting once again the ISO capability along with the presence of crystalline silicate complexes. As a matter of fact, the detection limit of ISO for broad spectral features is around 5% of the continuum level, depending on the quality of the spectrum. That we clearly recognise several intense crystalline profiles defines a lower limit for the crystallinity (defined as the ratio between the total mass of crystalline silicates over the silicate total mass) and, in turn, an acceptable approximate range for the mass-loss rate (Kemper et al. 2001). In particular, the ratio of the ∼33 μm fosterite band over the continuum (∼0.4) allows us to suggest that the fosterite mass fraction is greater than 0.15 and that the cool component of the symbiotic star HD 330036 loses mass at a rate of $\sim 0.4-1 \times 10^{-6}\ M_\odot$/yr (see Fig. 7 of Kemper et al. 2001). Unfortunately the ∼43 μm enstatite band is located just to the upper edge of the SWS spectrum, and its exact profile is more ambiguous; nonetheless, a raw estimate of its relative intensity seems to support our evaluation of the HD 330036 cool component mass loss.

5.3.5. Crystallisation processes

The crystalline grains require a high temperature and a low cooling rate for annealing. Molster et al. (1999a) suggested that the crystallisation of silicates in the outflow sources takes place close to the star, i.e. at high temperatures, whereas in a long-term stable disk, crystallisation occurs slowly at low temperatures

under the influence of UV radiation (Sylvester et al. 1999). The temperature required for an effective annealing (∼1000 K) that would last long enough to activate the crystallisation process can be reached both in the inner region of the outflowing envelope of cool component stars and in the expanding shocked nebula of SS, where colliding winds enable shock waves to compress and heat the dust grains. In effect, the shocks could be a very suitable mechanism thanks to the sudden heating and gradual cooling of the grains in the post-shock region, favouring the annealing processes and, in this way, initialising the crystallisation path. Such a mechanism has already been suggested with the purpose of explaining the formation of crystalline grains within comets in the protoplanetary solar nebula (Harker & Desch 2002) and it suggests a non secondary role of shocks in the dust transformation processes and consequent infrared emission feature.

Our models show that at typical expansion velocities of $\sim$15−20 km s^{-1}, the dust grains formed at $T \sim 1000$ K would spend 160−320 d at temperatures higher than 900 K, period that is long enough for the annealing and the subsequent crystallisation of a significant portion of dust grains. The crystallisation process will occur within a distance of $\sim 10^{14}$ cm, which agrees with the size of the outer dust shells.

On the basis of the theoretical silicate evolution index (SEI) proposed by Hallenbeck et al. (2000) and the insight of Harker & Desch (2002), we thus suggest that crystallisation processes in HD 330036 are triggered by shocks and that annealing takes place within the circumbinary disk.

6. Discussion and concluding remarks

The analysis of the D' type symbiotic system HD 330036 has been presented by modelling the continuum SED, along with the line and dust spectra within a colliding-wind binary scenario (Sect. 2). The framework is further complicated in D' type systems by the rapid rotation of the cool component, which strongly affects the symbiotic environment, leading to a disk-like circumbinary structure where the high gas density enhances grain formation and growth.

We have found (Sect. 3) that the UV lines are emitted from high-density gas between the stars downstream of the reverse shock, while the optical lines are emitted downstream of the shock propagating outwards the system. The models that best explain both the observed UV and optical line ratios correspond to $T_* = 60\,000$ K: regarding the gas density, in the downstream region of the reverse shock it reaches 10^8 cm^{-3}, while it is $\sim 10^6$ cm^{-3} downstream of the expanding shock. Free-free radiation downstream of the reverse shock is self-absorbed in the radio, so the data in that range are explained by bremsstrahlung from the nebula downstream of the expanding shock, which becomes optically thick at $\nu \leq 5$ GHz.

The relative abundances of C, N, and O adopted to reproduce the UV line ratios are in good agreement with those obtained by SN93 for symbiotic stars. Particularly, C/O = 0.70 indicates a carbon enrichment of the cool star, which can be explained by the transpher of matter from the hot component, a carbon star before becoming a WD. This hypothesis, suggested by SN93, along with the CIII] 1909/SiIII]1892 ratio <1 predicted by the models, favours classification of HD 330036 as a SS more than a PN.

The SED of the continuum (Sect. 4) has been disentangled in the different gas and dust contributions: the star fluxes, bremsstrahlung radiation, and reprocessed radiation by dust from the shocked nebulae. Throughout the modelling, we considered silicate grains with $a_{\rm gr} = 0.2\ \mu$m, which correspond to the size of grains generally present in the ISM, and large grains with $a_{\rm gr} = 2.0\ \mu$m, which are suitable to become crystalline.

Three shells are identified in the continuum IR SED, at 850 K, 320 K, and 200 K with radii $r = 2.8 \times 10^{13}$ cm, 4×10^{14} cm, and 10^{15} cm, respectively, adopting a distance to Earth $d = 2.3$ kpc. Interestingly, all these shells appear to be circumbinary.

The consistent modelling of line and continuum emission in the shocked nebulae leads to relatively low dust-to-gas ratios, particularly for large grains. Comparing with D-type SS that are generally rich in dust, HD 330036 shows d/g lower by factors >10. Dust-reprocessed radiation at ≤100 K downstream of the shock propagating outwards the system cannot be seen in the SED because hidden by the dust shell radiation flux.

The analysis of the ISO-SWS spectrum (Sect. 5) has revealed that both PAHs and crystalline silicates coexist in HD 330036. We suggest that the PAHs are associated with the internal shell at 850 K, while crystalline silicates, which derive from annealing of amorphous silicates at temperatures ≥1000 K, are now stored in the cool shells at 320 K and 200 K. Strong evidence that crystalline silicates are in a disk-like structure is derived on the basis of the relative band strengths.

The proposed scenario would link HD 330036 to some bipolar Post-AGB stars that have shown this sort of dichotomy in the dust composition, location, and geometrical distribution (Molster et al. 2001; Matsuura et al. 2004).

The presence of such strong crystalline features is intriguing in the light of our colliding-wind model; for example, the temperature required for an effective annealing that is long enough to activate the crystallisation process could be reached in the expanding nebula of SS, where colliding winds enable shock waves to compress and heat the dust grains. The shocks may represent a very suitable mechanism for triggering the crystallisation processes, principally thanks to the sudden heating and gradually cooling of the grains in the post-shock region, which might favour the annealing processes. We thus suggest that the crystallisation processes in HD 330036 may be triggered by shocks and that annealing may take place within the circumbinary disk.

Our scenario is schematic, of course, and should be considered as a mere approximation of the actual physical picture. New observations have been revealing the high complexity of these symbiotic environment, where the dynamic of binary components as a key parameter is not so trivial as to be disregarded entirely. The VLTI/MIDI proposal (P. I. D'Onofrio – 079.D-0242) based on our model and recently accepted by ESO aims to unveil the HD 330036 dust environment by means of IR interferometric observations, constraining the morphology and the emitting properties of the PAH-dust shell.

Acknowledgements. The authors would like to thank A. Cicakova for reading the manuscript. R.A. acknowledges the kind hospitality of the School of Physics & Astronomy of the Tel Aviv University.

References

Achmad, L., Lamers, H. J. G. L. M., & Pasquini, L. 1997, A&A, 320, 196
Allamandola, L. J., Tielens, G. G. M., & Barker, J. R. 1989, ApJS, 71, 733
Allen, C. W. 1973, Astrophysical Quantities (London: Athlon)
Allen, D. A. 1982, ASSL 95, The Nature of Symbiotic Stars, IAU Colloq., 70, 27
Allen, D. A. 1984, Ap&SS, 99, 101
Anandarao, B. G., Taylor, A. R., & Pottasch, S. R. 1988, A&A, 203, 361
Angeloni, R., Contini, M., Ciroi, S., & Rafanelli, P. 2007a, AJ, 134, 205
Angeloni, R., Contini, M., Ciroi, S., Rafanelli, P. 2007b, A&A, accepted
Bakes, E. L. O., Tielens, A. G. G. M., & Bauschlicher, C. W., Jr. 2001, ApJ, 556, 501

Barker, J. R., Allamandola, L. J., & Tielens, A. G. G. M. 1987, ApJ, 315, L61
Belczyński, K., Mikołajewska, J., Munari, U., Ivison, R. J., & Friedjung, M. 2000, A&AS, 146, 407
Bhatt, H. C. 1989, A&A, 214, 331
Bhatt, H. C., & Mallik, D. C. V. 1986, A&A, 168, 248
Chiar, J. E., Peeters, E., & Tielens, A. G. G. M. 2002, ApJ, 579, L91
Contini, M. 1997, ApJ, 483, 887
Contini, M. 2003, MNRAS, 339, 125
Contini, M., & Formiggini, L. 1999, ApJ, 517, 925
Contini, M., & Formiggini, L. 2001, A&A, 375, 579
Contini, M., & Formiggini, L. 2003, MNRAS, 339, 148
Contini, M., & Prialnik, D. 1997, ApJ, 475, 803
Contini, M., Collodel, L., & Rafanelli, P. 1997, Astronomical Time Series, ASSL, 218, 203
Contini, M., Viegas, S. M., & Prieto, M. A. 2004, MNRAS, 348, 1065
Corradi, R. L. M., Brandi, E., Ferrer, O. E., & Schwarz, H. E. 1999, A&A, 343, 841
Cox, D. P. 1972, ApJ, 178, 143
Crocker, M. M., Davis, R. J., Eyres, S. P. S., et al. 2001, MNRAS, 326, 781
de Graauw, T., Haser, L. N., Beintema, D. A., et al. 1996, A&A, 315, L49
Feast, M. W., Catchpole, R. M., Whitelock, P. A., Carter, B. S., & Roberts, G. 1983, MNRAS, 203, 373
Feibelman, W. A. 1983, ApJ, 275, 628
Feibelman, W. A. 1988, A Decade of UV Astronomy with the IUE Satellite, 2, 179
Formiggini, L., Contini, M., & Leibowitz, E. M. 1995, MNRAS, 277, 1071
Girard, T., & Willson, L. A. 1987, A&A, 183, 247
Hallenbeck, S. L., Nuth, J. A., III, & Nelson, R. N. 2000, ApJ, 535, 247
Harker, D. E., & Desch, S. J. 2002, ApJ, 565, L109
Hony, S., Van Kerckhoven, C., Peeters, E., et al. 2001, A&A, 370, 1030
Hudgins, D. M., & Allamandola, L. J. 1999, ApJ, 513, L69
Joblin, C., D'Hendecourt, L., Leger, A., & Defourneau, D. 1994, A&A, 281, 923
Joblin, C., Boissel, P., Leger, A., D'Hendecourt, L., & Defourneau, D. 1995, A&A, 299, 835
Kemper, F., Waters, L. B. F. M., de Koter, A., & Tielens, A. G. G. M. 2001, A&A, 369, 132
Kenny, H. T., & Taylor, A. R. 2005, ApJ, 619, 527
Kenyon, S. J. 1988, AJ, 96, 337
Kharchenko, N. V. 2001, Kinematika i Fizika Nebesnykh Tel, 17, 409
Lutz, J. H. 1984, ApJ, 279, 714
Matsuura, M., Zijlstra, A. A., Molster, F. J., et al. 2004, ApJ, 604, 791
Milne, D. K., & Aller, L. H. 1982, A&AS, 50, 209
Molster, F. J., Yamamura, I., Waters, L. B. F. M., et al. 1999, Nature, 401, 563
Molster, F. J., Yamamura, I., Waters, L. B. F., et al. 2001, A&A, 366, 923
Molster, F. J., Waters, L. B. F. M., Tielens, A. G. G. M., & Barlow, M. J. 2002a, A&A, 382, 184
Molster, F. J., Waters, L. B. F. M., & Tielens, A. G. G. M. 2002b, A&A, 382, 222
Molster, F. J., Waters, L. B. F. M., Tielens, A. G. G. M., Koike, C., & Chihara, H. 2002c, A&A, 382, 241
Munari, U., Tomov, T., Yudin, B. F., et al. 2001, A&A, 369, L1
Nussbaumer, H. 2000, Thermal and Ionisation Aspects of Flows from Hot Stars, ASP Conf. Ser., 204, 317
Nussbaumer, H., & Walder, R. 1993, A&A, 278, 209
Nussbaumer, H., Schmutz, W., & Vogel, M. 1995, A&A, 293, L13
Osterbrock, D. E. 1988, in Astrophysics of Gaseous Nebulae and Active Galactic Nuclei (University Science Book)
Peeters, E., Hony, S., Van Kerckhoven, C., et al. 2002, A&A, 390, 1089
Pereira, C. B., Smith, V. V., & Cunha, K. 2005, A&A, 429, 993
Puget, J. L., & Leger, A. 1989, ARA&A, 27, 161
Roche, P. F., Aitken, D. K., & Allen, D. A. 1983, MNRAS, 204, 1009
Schild, H., Eyres, S. P. S., Salama, A., & Evans, A. 2001, A&A, 378, 146
Schmeja, S., & Kimeswenger, S. 2001, A&A, 377, L18
Schmid, H. M., & Nussbaumer, H. 1993, A&A, 268, 159
Schulte-Ladbeck, R. E., & Magalhaes, A. M. 1987, A&A, 181, 213
Sloan, G. C., Kraemer, K. E., Price, S. D., & Shipman, R. F. 2003, ApJS, 147, 379
Smith, V. V., Pereira, C. B., & Cunha, K. 2001, ApJ, 556, L55
Soker, N. 2002, MNRAS, 337, 1038
Sylvester, R. J., Kemper, F., Barlow, M. J., et al. 1999, A&A, 352, 587
van Diedenhoven, B., Peeters, E., Van Kerckhoven, C., et al. 2004, ApJ, 611, 928
Van Winckel, H., Schwarz, H. E., Duerbeck, H. W., & Fuhrmann, B. 1994, A&A, 285, 241
Vandenbussche, B., Dominik, C., Min, M., et al. 2004, A&A, 427, 519
van Loon, J. T., Cioni, M.-R. L., Zijlstra, A. A., & Loup, C. 2005, A&A, 438, 273
Viegas, S. M., & Contini, M. 1994, ApJ, 428, 113
Wachter, A., Schröder, K.-P., Winters, J. M., Arndt, T. U., & Sedlmayr, E. 2002, A&A, 384, 452
Webster, B. L., & Allen, D. A. 1975, MNRAS, 171, 171
Williams, R. E. 1967, ApJ, 147, 556
Yamamura, I., Dominik, C., de Jong, T., Waters, L. B. F. M., & Molster, F. J. 2000, A&A, 363, 629
Zamanov, R. K., Bode, M. F., Melo, C. H. F., et al. 2006, MNRAS, 365, 1215